Design of Highly Efficient Electronic Energy Transfer in Functionalized Quantum Dots Drived Specifically by Ethylenediamine

Wenfei Ren,[a,b,‡] Jiguang Li,[a,‡] Baiyi Zu,[a,c,*] Da Lei,[a,c] and Xincun Dou[a,b,c,*]

[a] Xinjiang Key Laboratory of Trace Chemicals Sensing, Xinjiang Technical Institute of Physics & Chemistry, Chinese Academy of Sciences, Urumqi 830011, China

[b] Center of Materials Science and Optoelectronics Engineering, University of Chinese Academy of Sciences, Beijing 100049, China

[c] Key Laboratory of Improvised Explosive Chemicals for State Market Regulation, Urumqi 830011, China

KEYWORDS EDA; EET; Fluorescence; QDs; Explosive

ABSTRACT: The exploring of emerging functionalized quantum dots (QDs) through modulating the effective interaction between the sensing element and target analyte is of great significance for high-performance trace sensing. Here, the chromone-based ligands grafted QDs (QDs-Chromone) were initiated to realize the electronic energy transfer (EET) drived specifically by ethylenediamine (EDA) in the absence of spectral overlap. The fluorescent and colorimetric dual-mode responses (from red to blue and from colorless to yellow, respectively) resulted from the expanded conjugated ligands reinforced the analytical selectivity, endowing an ultrasensitive and specific response to submicromolar-liquid of EDA. In addition, a QDs-Chromone-based sensing chip was constructed to achieve the ultrasensitive recognition of EDA vapor with a naked-eye observed response at a concentration as low as 10 ppm, as well as a robust anti-interfering ability in complicated scenarios monitoring. We expect the proposed EET strategy in shaping functionalized QDs for high-performance sensing would shine light on both rational probe design methodology and deep sensing mechanism exploration.

INTRODUCTION

Amines generally play critical roles in chemical engineering,[1] biological inspection[2] and industrial production[3] owing to their alkaline and nucleophilic characteristics as well as the excellent water solubility, nevertheless, the highly toxic amines and amine vapors would cause huge damage to environment and threaten the health of human beings.[4-5] Furthermore, amines could be taken as the nitrogen source for nitrogenous explosive, and thus are easily employed as the raw materials of improvised explosive devices (IEDs). As one of the most representative example of it, ethylenediamine (1,2-diamines, EDA), is one of the primary ingredients used to make the powerful Picatinny liquid explosive.[6] As a typical amine compound, EDA has the typical characteristics of amines (alkalinity and nucleophilicity) as well as corrosivity and toxicity, and due to this reason, WHO has specified 10 ppm as the occupational exposure limit of EDA.[6-7] Therefore, it is important to develop highly selective, highly sensitive and rapid response methodologies for on-site EDA detection.[8-12] Apparently, especially in resource-limited areas, the detection of EDA has been trending away from bulky and time-consuming instruments as well as complex detecting procedures, which needs to be carried out at designated laboratories with trained personnel in most cases.[13-17] Thus, optical method is considered as one of the most promising approaches for on-site EDA sensing coupled with image analysis techniques because of its visual (with naked-eye) and real-time measurement results, easy operating and portable characteristics.[18-21] For instance, Lin et al. realized a reversible selective fluorescent response for EDA by pillar[5]arene-based crystalline material (PQ8),[22] although the form of fluorescence quenching made it difficult for naked eye to resolve the concentration of EDA. Huang et al. reported nonporous adaptive pillar[4]arene[1]quinone crystals for fluorescence turn-on sensing of EDA vapor,[23] while the sensitivity and response time still need to be improved. Although significant advances have been achieved in the design of optical detection strategies of EDA, the limit in this area is still obvious, such as the complicated synthesis procedures of probes, the bad photostability of the probes, the inefficient response mode, long response time, poor selectivity and sensitivity.[24-25] Therefore, it has aroused the pressing need to develop rapid and accurate optical detection strategies to EDA with stable probes, as well as a detection mode that is friendly to on-site naked eye observation.

With superior optical features and unrivaled photostability luminescence, quantum dots (QDs) have been widely utilized not only for photophysics but also for biological and chemical applications in recent years.[26-28] At the same time, due to the versatile surface chemistry feature, QDs have already been demonstrated to be efficient energy transfer (ET) donors or acceptors, enabling specific detection toward target analytes through the grafting of de-

signed ligands.[29-31] Up to now, most of the existing QDs detecting system were conceptualized based on Förster resonance energy transfer (FRET),[32] photoinduced electron transfer (PET),[33] inner filter effect (IFE),[34] or combination with each other.[35] For example, Wang et al. reported a rapid and sensitive platform for the quantitative analysis of dopamine based on boronic acid-functionalized molybdenum disulfide quantum dots (B-MoS_2 QDs) owing to the IFE and the aggregation quenching effect,[36] although the fluorescence "off" exhibited by IFE would easily be interfered by a series of factors in on-site scenarios. Su et al. constructed the FRET system between CdTe QDs and Rhodamine B (RB) for the ratio fluorescent detection of melamine,[37] in which the fluorescence intensity of the RB decreased faster than that of CdTe QDs with the addition of melamine. Generally, compared to the appearance or decrease of a single emission signal, ET based probes typically have two emission peaks, which make internal referencing of the signal possible.[38] And as one of the most typical ET process, FRET usually requires the following four conditions to achieve a satisfying signal: (i) a donor with a high quantum yield; (ii) a spectral overlap of the donor emission with the acceptor absorption; (iii) an appropriate relative orientation of the transition dipoles and (iv) a close enough donor-acceptor distance (typically less than 10 nm).[27] These critical requirements severely hindered the exploration of new functionalized QDs based on the energy transfer mechanism, and thus is not favorable for the development of highly efficient sensing methodology. Considering that the energy transfer may take place even in the absence of spectral overlap,[39] electronic energy transfer (EET), derived from (i) long-range resonance, or through-space ET, (ii) short-range wave function overlap or through-bond mechanisms or (iii) super exchange bridge-mediated mechanism,[40-41] could be a more versatile and promising mechanism being employed in the exploration of high-performance sensing method. However, as far as we known, this important EET mechanism has not been employed in the area of analytical chemistry, not to mention that whether a sensing model could be initiated through the design of functionalized QDs and the effective interaction with the target analyte.

Herein, as proof-of-concept demonstrations of electronic energy transfer in the ultrasensitive and specific detection of trace analyte with fluorescent and colorimetric dual-mode responses, a specially functionalized QDs was designed and showed highly efficient EET from QDs to the ligands drived specifically by EDA. It should be noted that, generally, EET between the donor (D) and the acceptor (A) chromophoric units is usually induced by (sun)light accompanying with the transfer and the separation of electrons and holes after excitation (Scheme 1a-i), which is usually applied in the photophysical, artificial photosynthetic, photovoltaic systems.[40-42] Here, we propose another kind of EET, driving by analytes and accompanying with the production of new compounds. It is noteworthy that the transfer of electrons and holes of the present EET occurs both in the excited states (Scheme 1 a-ii). As a result, the previous EET exhibits the fluorescence of the acceptor (A), while the present EET exhibits the obvious change in fluorescence, which behaves as the quenching of the donor's fluorescence and the increasing of the acceptor's fluorescence (Scheme 1b). Based on the nucleophilicity of EDA as well as the stable intramolecular hydrogen bonds between chromone and primary amines,[43-46] CdSe/ZnS QDs with red emission were grafted with chromone-based ligands to form a probe (QDs-Chromone) with electrons and holes localized in the QDs. While triggered by EDA through the nucleophilic addition with the ligands, the electrons and holes would shift and preferentially localized in the ligands afterwards. The QDs-Chromone designed accordingly demonstrated bright blue fluorescence and yellow color change towards EDA with ultrasensitivity (limit of detection, defined as LOD, of 0.11 μM and 2.94 μM in fluorescent and colorimetric mode, respectively, as well as a naked-eye observed change for 10 ppm EDA vapor), and great specificity compared with the structural analogues (various amines) and other common interferents. Given the above, as a more versatile and promising mechanism initiated through the functionalized QDs and the valid interaction with the target analyte, it is expected that EET would certainly renew the existing design strategies for trace sensing.

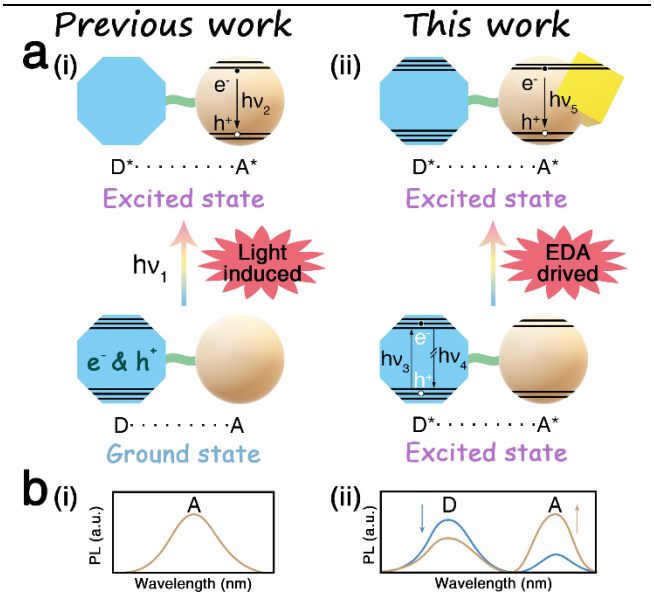

Scheme 1. (a) Light induced (i) and analytes drived (ii) EET process. (b) The fluorescence results of these two kinds of EET.

RESULTS AND DISCUSSION

Principle of the EET Detection System. Based on the nucleophilicity of EDA, QDs is designed to contact with an electron donor (Figure 1a),[30] which results in the generation of holes and the sites that are easy for nucleophile to attack in ligands. The electrostatic potential (ESP) distribution diagram shows that the C atom at β position of the carbonyl group has the positive electrostatic potential with a value of 15.79 kcal/mol due to the electrophilic effect of QDs (Figure 1b), which may show good affinity and selectivity toward primary amines.[43-44] Here, a functionalized CdSe/ZnS QDs (donor) emit red fluorescence and grafted with chromone-based molecules (acceptor) by Zn–S bond were constructed, and with the help of the target analyte molecules, the specific EET for sensing was realized (Figure 1c). It should be noted that in order to stabilize and

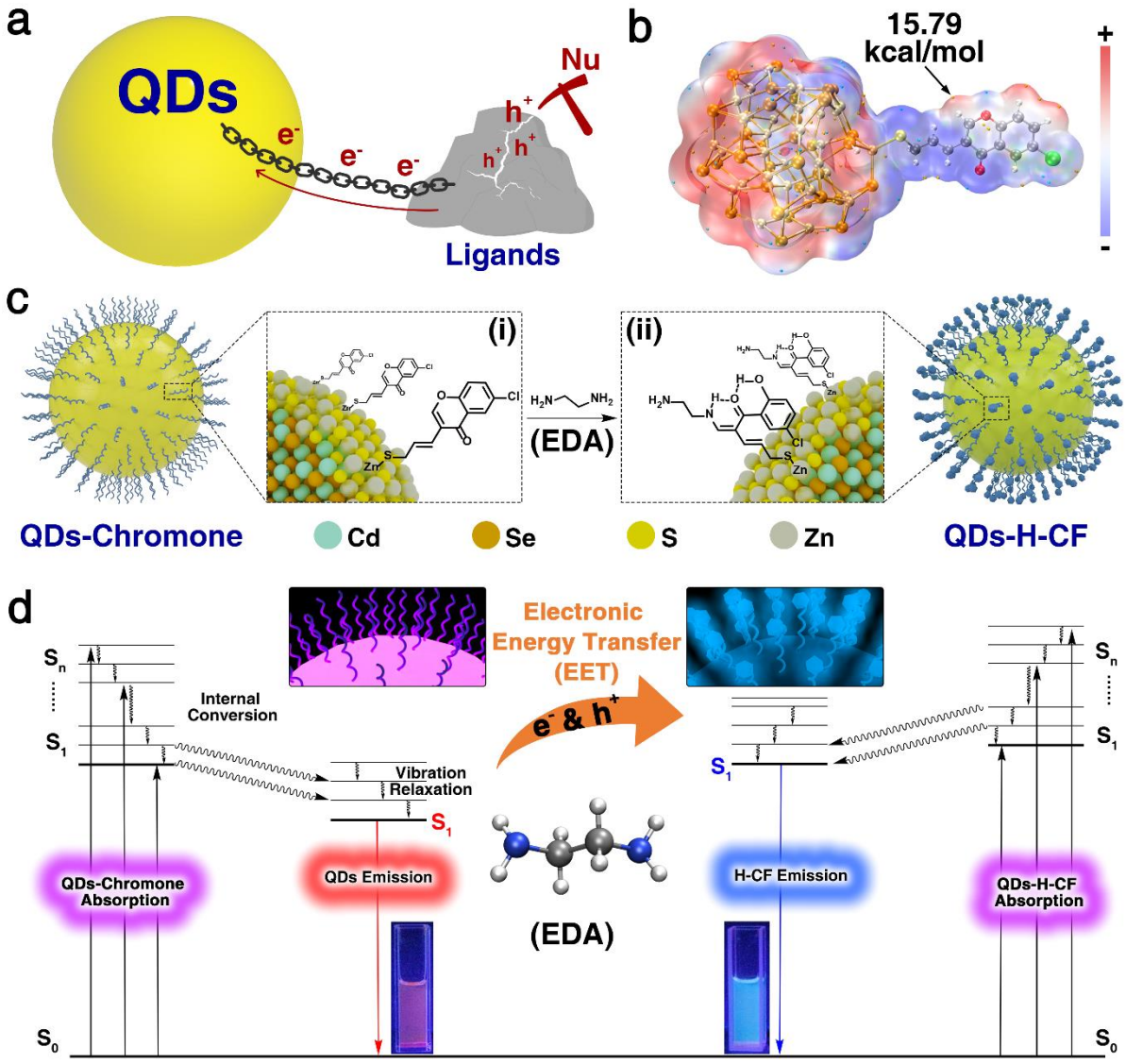

Figure 1. (a) Schematic illustration of electrophilic effect of QDs and nucleophilic (Nu) attack. (b) The electrostatic potential (ESP) distribution diagram of the QDs-Chromone molecule, in which the maximal and minimum ESP surfaces presented as orange and cyan dots, respectively. (c) Schematic illustration and (d) Jablonski diagram and the corresponding fluorescence emission images of the QDs-Chromone before and after detecting EDA.

maximize fluorescence in practical application, it is favorable to coat emitting core (CdSe) with an insulating inorganic and large band gap shell (ZnS), which insulates the core, passivates the surface bonds, reduces the toxicity, and buries the QDs in a potential energy well.[47] After detection of EDA, the C–O bonds would be broken and two kinds of hydrogen bonds (N–H···O and O–H···O) would be formed, resulting in the expansion of the conjugate plane structure[43-44] to emit blue fluorescence (Figure 1c-ii). The expanded conjugated fluorophores grafted on CdSe/ZnS QDs were thus named as QDs-H-CF.

To better understand the corresponding EET mechanisms in this scheme, the different electronic states and the transition processes of the QDs-Chromone and QDs-H-CF were elucidated in a Jablonski diagram[48] (Figure 1d). The QDs-Chromone absorbs photon energy under UV light, and is excited with electron elevation and a change in the electronic state from the ground state (S_0) to a singlet excited state (S_n). And then, after a rapid internal conversion process and vibration relaxation, the QDs-Chromone reaches to the lowest singlet excited state (S_1) and its energy would mostly dissipate through emit the QDs' intrinsic red fluorescence (left in Figure 1d). While after detection of EDA, the system's energy would mostly dissipate in the form of blue fluorescence originating from the ligands, and this emission change is certainly derived from the effective electronic energy transfer from QDs to the ligands afterwards due to the special QDs-Chromone design (right in Figure 1d). Different from PET or FRET, EET usually happens when the electron and the hole of donor simultaneously transfer to the acceptor's LUMO/CB and HOMO/VB respectively after excitation, and as a result, the fluorescence of the donor quenches while that of the acceptor increases.

Characterization and Mechanism of the QDs-Chromone before and after Detection of EDA. The as-prepared CdSe/ZnS QDs (QDs-OA) according to the previous report[49] with oleic acid (OA) grafted on the surface were then further modified by ligand exchange with hydrophilic mercaptopropionic acid (MPA) to replace OA to

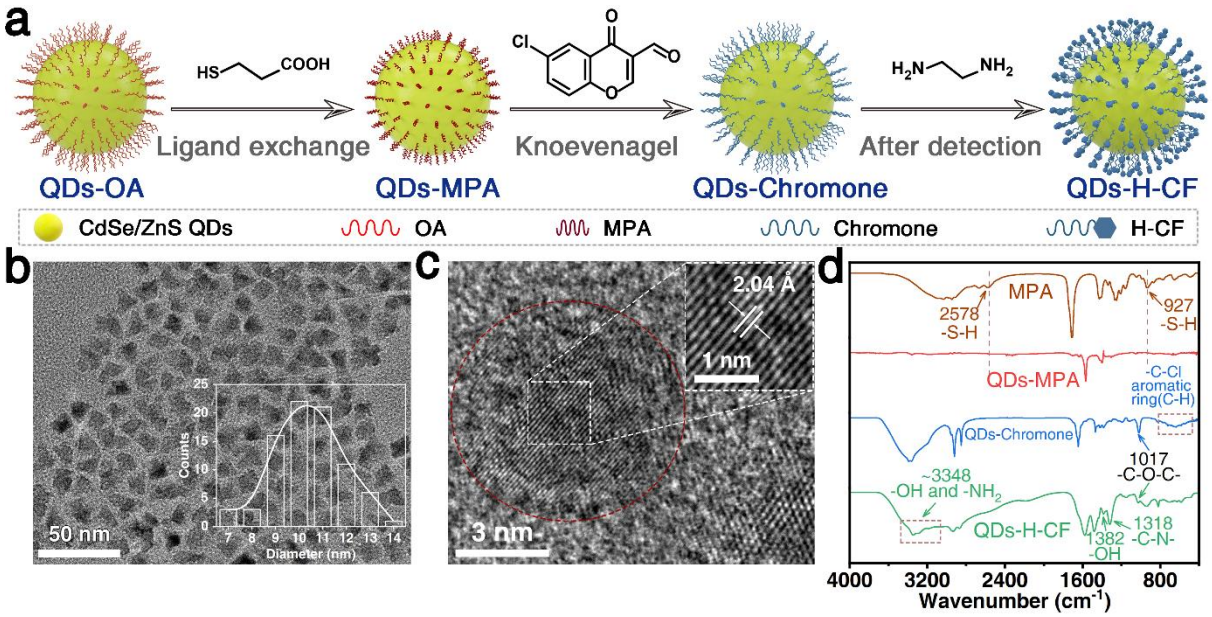

Figure 2. (a) Schematic illustration of the CdSe/ZnS QDs modification and detection. (b) TEM image of the QDs-OA. (Inset: the corresponding size distribution). (c) HRTEM images of the QDs-OA. (d) FT-IR spectra of the QDs-OA, MPA, QDs-MPA, QDs-Chromone and QDs-H-CF.

improve the solubility in aqueous media. The obtained QDs-MPA was used for reacting with the chromone compound by Knoevenagel condensation to get the specific probes (QDs-Chromone) for detecting EDA, which was then reacted with EDA to result in the change of the ligand and finally form the reaction product QDs-H-CF (Figure 2a and S1).

The homogeneous and triangular morphology as well as the dispersion of the QDs-OA with an average diameter of 10–11 nm is verified by transmission electron microscopy (TEM) characterization (Figure 2b). The clear lattice fringes in the high-resolution TEM (HRTEM) images indicate the good crystallinity of the QDs-OA, and the lattice spacing of 2.04 Å corresponds well with the (220) lattice of CdSe[50] (Figure 2c). The appearance of the QDs-OA shows no change through the following two modification steps (Figure S2), indicating the superior stable feature of the QDs. Fourier transform infrared (FT-IR) spectroscopy analysis confirms that the shedding of OA is due to the disappearance of the absorption peaks around 2920 cm^{-1}, which corresponds to the stretching vibration of the $-CH_2-$. And the QDs are grafted with MPA by thiol groups due to the disappearance of the absorption peaks at 2578 cm^{-1} and 927 cm^{-1}, corresponding to the stretching vibration and bending vibration of S–H, respectively (gray, brown and red line in Figure 2d). At the same time, the appearance of the absorption peak at 1017 cm^{-1} and the broad peak around 470–800 cm^{-1}, corresponding to the stretching vibration of C–O–C and the bending vibration of C–Cl as well as C–H on the aromatic ring (blue line in Figure 2d), demonstrates the successful synthesis of the QDs-Chromone. And thin-layer chromatography plate certifies the ingredients and the by-products have been successfully separated from the QDs-Chromone (Figure S3). After detection of EDA, the appearance of the broad peak around 3348 cm^{-1} of the amidogen indicates the addition of EDA, while the weakened peak of C–O–C (1017 cm^{-1}) and the appearance of O–H (1382 cm^{-1}) as well as C–N (1318 cm^{-1}) confirm the broken of the C–O bonds and the reaction of QDs-Chromone with EDA (green line in Figure 2d).

The comparison of the corresponding X-ray photoelectron spectroscopy (XPS) of the QDs-Chromone before and after detection of EDA verified the presence of Cd, Cl and N, which also indicated the successful synthesis of QDs-Chromone and the reaction of QDs-Chromone with EDA, respectively (Figure S4a). The high-resolution XPS spectrum of the N 1s (Figure S4b) can be fitted with two main components with peaks at 398.78 eV and 399.48 eV, corresponding to N–H and C–N, respectively.[51-52] After detection of EDA, the appearance of C–N and N–H along with the obvious decrease of C–O–C as well as the increase of C–OH indicates the broken of C–O bonds and the generation of C–N (Figure S4c-f), which agrees well with the results of FT-IR analysis. Combined with the ^1H NMR spectra of the QDs-OA, QDs-MPA, QDs-Chromone and after addition of two different concentrations of EDA (Figure S5), the obvious reduction of the signals of H in the alkyl chain around δ 1.3 also indicates the shedding of OA. Furthermore, the successful synthesis of the QDs-Chromone is verified by the appearance of H in the aromatic ring within δ 7.5–9. Moreover, the signals of H in the aromatic ring shift to the upper field (from around δ 8 to around δ 7), and the appearance of H in the amidogen around δ 3 indicates the ring cleavage and the formation of the hydrogen bonds (N–H···O and O–H···O) which resulted in the expansion of the conjugate plane structure.[53] Subsequently, the tiny emission band change of QDs before and after modification of MPA and chromone, together with the appearance of fluorescence intensity in low wavelength region of QDs-Chromone verify the successful modification from another aspect, which also bring out the change of fluorescence from bright red to dark red and purple (Figure S6). In addition, the different fluorescence lifetimes of QDs-MPA, and QDs-Chromone before and after the binding of EDA (9.98 ns, 12.86 ns and 2.43 ns, respectively), clearly indicate the successful modification and the formation of different ligands on the QDs.

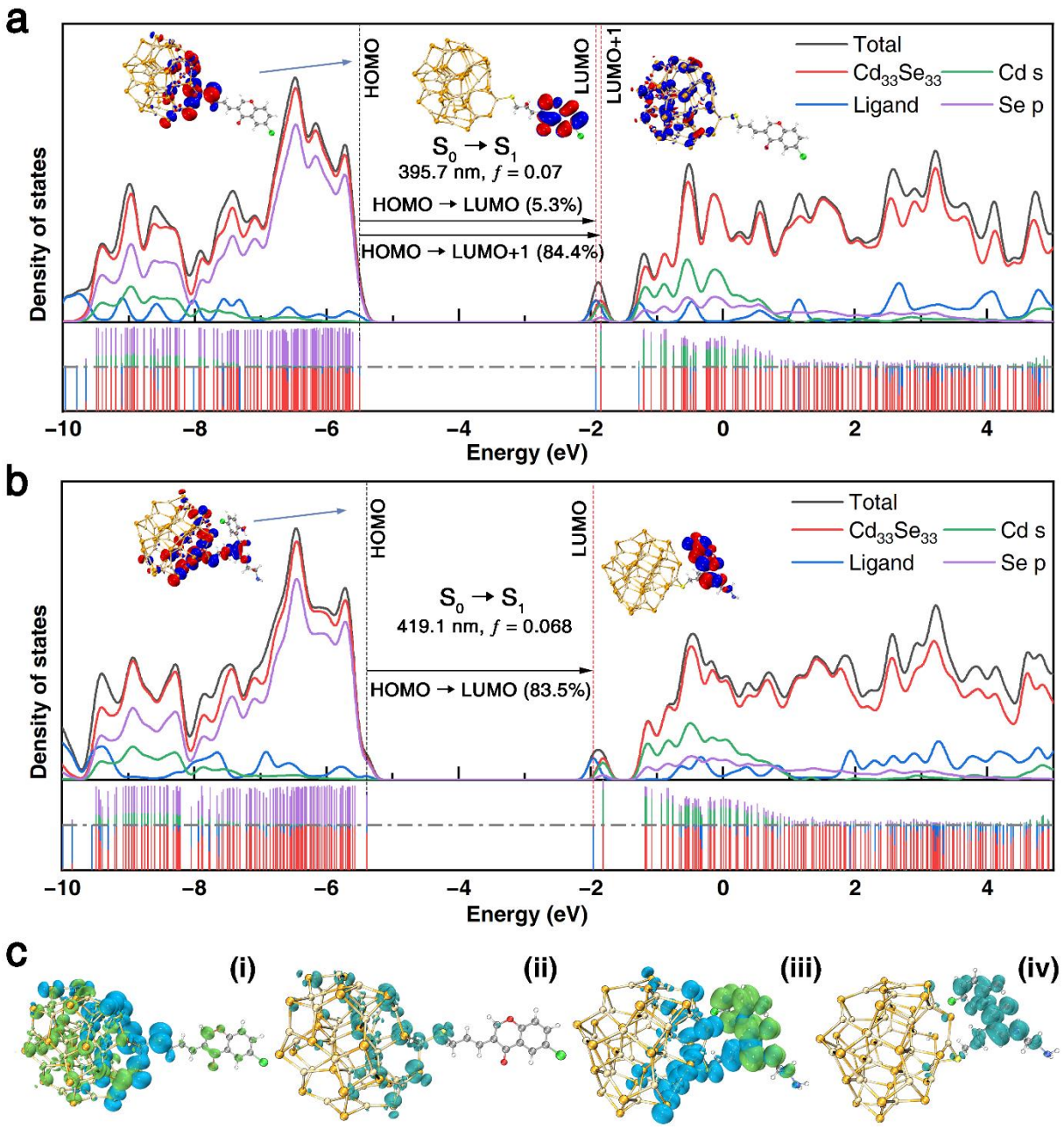

Figure 3. (a) The density of states (DOS) and projected density of states (PDOS) of the QDs-Chromone. Inset: surface plots of the HOMO, LUMO and LUMO+1 (isovalue = 0.02). (b) The DOS and PDOS of the QDs-Chromone after EDA detection. Inset: surface plots of the HOMO and LUMO (isovalue = 0.02). (c) Real space representation of hole and electron distributions (i) before and (iii) after EDA detection: green and blue regions denote the hole and electron distributions (isovalue = 0.0005), respectively, and real space representation of hole and electron overlapping region distribution (ii) before and (iv) after EDA detection.

Thus, it is powerfully proved that the detection phenomenon is caused by the occurrence of EET, rather than the production of a new fluorophore upon the interactions between EDA and the chromone group (Figure S7).

Electronic Structure of QDs-Chromone and QDs-H-CF. It should be noted that as a common model of QDs in quantum-chemical simulations,[54] the ZnS shell is often ignored to reduce the computational effort, and a ~1.3 nm $Cd_{33}Se_{33}$ quantum dot (QD) was constructed with approximately spherical shapes and optimized to geometries with the lowest number of dangling bonds. The density of states (DOS) and projected density of states (PDOS) of the relaxed $Cd_{33}Se_{33}$ model QD ligated by a chromone molecule showed a clear energy gap separating the occupied molecular orbitals (MOs) from the unoccupied MOs (Figure 3a). The highest occupied molecular orbital (HOMO) and the next lower-energy occupied states formed a densely packed set of energy levels, while a noticeable energy gap separated the lowest unoccupied molecular orbital (LUMO) as well as the next higher-energy unoccupied state (LUMO+1) from the higher-energy unoccupied states. A decomposition of the different MOs into contributions from the atomic-like orbitals indicated that Se 4p states contributed mostly to the HOMO with a minor contribution from Cd 5s and the ligand orbitals, while the ligand orbitals contributed mostly to the LUMO and the Cd 5s states contributed mostly to the LUMO+1. A visualization of the MOs

of the HOMO, LUMO, and LUMO+1 (the inset in Figure 3a) showed that the HOMO localized over $Cd_{33}Se_{33}$ QD, and the LUMO localized over almost the entire ligand, while LUMO+1 localized over almost the entire $Cd_{33}Se_{33}$ QD. The fluorescence emission property of the QDs-Chromone was further approximated by the optical activity of the lowest singly excited transition according to the Kasha rule.[55] It is found that a vertical electron excitation energy at 395.7 nm with an oscillator strength (*f*) of 0.07 corresponds to an optically active state composed of HOMO → LUMO (5.3%) and HOMO → LUMO+1 (84.4%). This result suggests that the emission of the QDs-Chromone is optically active, and the fluorescence emission could be attributed to the significant transition from LUMO+1 to HOMO (84.4%) distributed both on $Cd_{33}Se_{33}$.

And then according to the Boltzmann conformation distribution based on Gibbs Free energy calculation, we explored the molecular conformational preferences of the chromone-ligands after detection of EDA. It is found that all the five lowest energy conformations have stable intramolecular hydrogen bonds between chromone and primary amines (Figure S8), while two of them (Figure S8a-b) are predominant (36.9% and 30%, respectively). It should be noted that it is also crucial to consider the formation of the stable intramolecular hydrogen bonds when optimizing the structure of QDs-H-CF based on PBE functional. The corresponding DOS and PDOS show a clear energy gap separating the occupied MOs from the unoccupied MOs at the PBE0/def2-SVP calculator level (Figure 3b). Similar with the characteristics of the MOs of the QDs-Chromone, the HOMO and the next lower-energy occupied states of QDs-H-CF formed a densely packed set of energy levels, while a noticeable energy gap separated the LUMO as well as LUMO+1 from the higher-energy unoccupied states. It is clearly shown that the Se 4p states predominantly contribute to the HOMO, while the ligand orbitals mainly contribute to the LUMO and the Cd 5s states primarily contribute to the LUMO+1. The HOMO also localizes over the $Cd_{33}Se_{33}$ QD, while the LUMO localizes over almost the entire ligand (the inset in Figure 3b). Upon comparison of the absorption of QDs-Chromone (395.7 nm, *f* = 0.07) and QDs-H-CF (419.1 nm, *f* = 0.068), although very close oscillator strength values are shown, there is still a wavelength shift of about 20 nm. Interestingly, the predominant HOMO → LUMO (83.5%) indicates that the emission of the QDs-H-CF is derived mostly from the ligands.

Due to the complexity of the electronic structure of the system, the S_1 state, which is extremely important for emission, cannot be simply expressed as a transition between a specific pair of MOs.[56] It is known that the hole-electron analysis can overcome this difficulty, thus, it is employed to investigate the characteristics of the electron energy transfer drived by EDA more comprehensively. In the QDs-Chromone, the electrons (blue regions) concentrate relatively on $Cd_{33}Se_{33}$ with a focus near the ligand, while the holes (green regions) delocalize on the entire QDs-Chromone structure (Figure 3c-i). It is shown that the overlapping region of the holes and electrons distribute on the $Cd_{33}Se_{33}$ (Figure 3c-ii), indicating that the oscillator strength (*f*) and thus the emission transition of the QDs-Chromone system is mainly contributed by QDs.[57] After reacting with EDA, the electrons (blue regions) concentrate in $Cd_{33}Se_{33}$ close to the ligand side as well as in the ligand, while all the holes (green regions) locate on the ligands (Figure 3c-iii). Thus, the overlapping region of the holes and electrons distribute on the ligand (Figure 3c-iv), indicating that the emission transition of the QDs-H-CF system is mainly contributed by the ligand. Therefore, from the quantum-chemical simulations of the electronic structures of the QDs-Chromone and QDs-H-CF, it is firmly proved that when drived by EDA, highly efficient EET would happen from the QDs to the ligand in this specially designed functionalized QDs system.

The Detection Performance of the QDs-Chromone toward EDA. Although the red fluorescence of the QDs itself remains unchanged after detection of EDA, the fluorescence of the excited QDs-Chromone changes from red to blue due to the expansion of the conjugate plane structure of ligands, and the color changes from almost colorless to yellow under natural light (Figure 4a). It is found that the fluorescence emission peaks of the QDs-MPA and 6-chloro-3-formylchromone in methanol solution appeared at 680 nm and 460 nm, respectively (Figure 4b). Thus, it is evidently proved that although the fluorescence spectrum of the red-emitting QDs (donor) has no spectral overlap with the absorption spectrum of the chromone compound (acceptor), efficient EET still occurs in QDs-Chromone after detection EDA.

As expected, a significant rise of the fluorescence intensity at 460 nm can be observed in the fluorescence intensity spectra with the addition of various concentrations (30-300 μm) of EDA, while the fluorescence intensities of the QDs at 680 nm almost remain unchanged (Figure 4c and S9). The variation of the fluorescence images shows a progressively emission color change trend from red to blue under irradiation with a 410 nm UV lamp (the inset in Figure 4c). In particular, 30 μm EDA can be completely distinguished from that observed in the absence of EDA. Furthermore, the absorption intensity at 436 nm also increases in the UV-vis spectra with the addition of various concentrations of EDA (Figure 4d and S10), and it becomes obvious when the EDA concentration reaches 160 μM. The increased absorption area suggests a gradual deepening color trend in the optical images from almost colorless, light yellow to yellow (the inset in Figure 4d). Based on these, the correlation between the enhanced fluorescence intensity at 460 nm as well as the absorption at 436 nm and the concentration of EDA is established (Figure 4e and Table S1−S2). The fitted curve exhibits a credible linearity when the EDA concentration varies from 0 to 300 μM, and the LOD (defined as LOD = 3σ/k, where k represents the slope of the fitted calibration curve with a value of 82.4828, and σ stands for the standard deviation of noise with a value of 3), is further obtained as 0.11 μM. Similarly, the absorption shows two linear optical behaviors with respect to the increasing EDA concentration in the range of 0−160 μM and 160−1000 μM, and the LOD is calculated based on the first linear interval as 2.94 μM according to 3σ/k with a σ of 0.0003. It should be noted that the almost unchanged fluorescence intensities of the QDs at 680 nm is due to the synergistic effect of the fluorescence quenching triggered by the EET mechanism and the fluorescence enh-

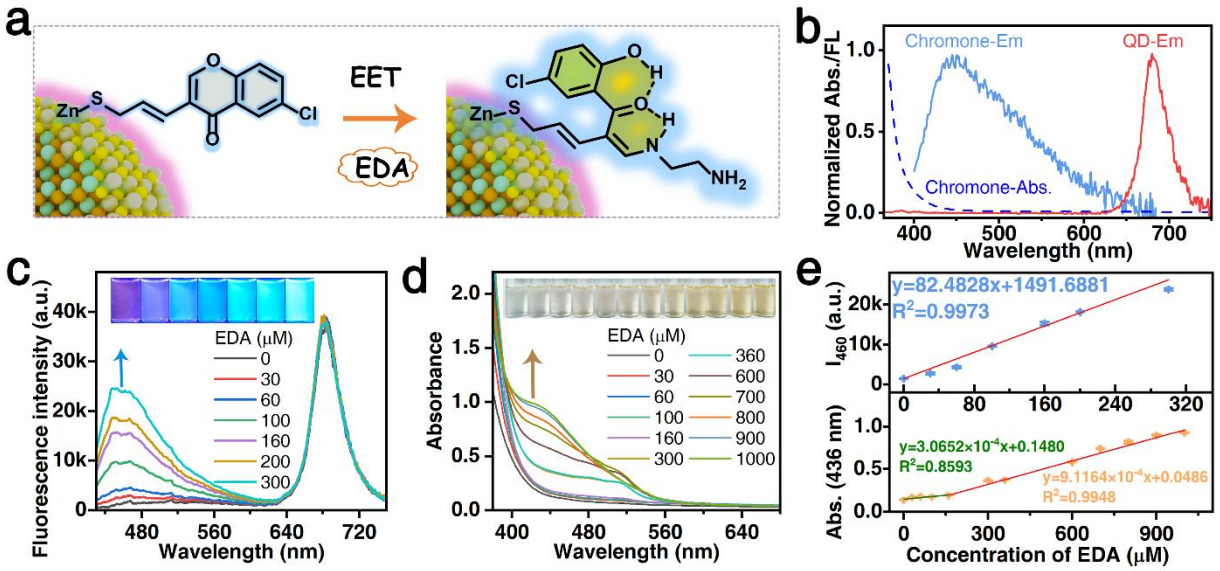

Figure 4. (a) Schematic representation of the QDs-Chromone used for sensing EDA. (b) Normalized spectra of the QDs-MPA emission (λ_{ex} = 410 nm, solid red line), 6-chloro-3-formylchromone absorption (dashed blue line) and emission (λ_{ex} = 378 nm, solid blue line). (c) Fluorescence spectra (λ_{ex} = 410 nm) and (d) UV-vis absorbance spectra obtained for the QDs-Chromone in response to different concentrations of EDA (0–300 μM and 0–1000 μM, respectively) and the corresponding images. (e) The fluorescence intensities at 460 nm and the absorption intensities at 436 nm with linearly fitted curves as a function of the EDA concentration.

ancement triggered by the generation of a new absorption band (purple region in Figure S11, 350 nm–546 nm), which closely aligns with the excitation wavelength of the QDs-Chromone (Figure S11). What's more, it is found that although the fluorescence intensity of 6-chlorochromone, a structurally similar substitute of the modified ligand, in response to different concentrations of EDA first increased and then decreased at 468 nm, the fluorescence intensity of QDs-Chromone after reacting with EDA at 460 nm is much stronger especially in the high EDA concentration range, indicating that the presence of the EET mechanism does play a vitally important role in promoting the detection performance toward EDA (Figure S12). In addition, the selectivity and sensitivity of the mixture of 6-chlorochromone and QDs-MPA are unsatisfying (Figure S13), which also imply that QDs do play an important electrophilic role in the system of QDs-Chromone in the nucleophilic addition. Thus, as a nucleophile substance, EDA would attack the C–O in the chromone ligand on the QDs easily, resulting the formation of the hydrogen bonds (N–H···O and O–H···O).

Based on the stability of the QDs-Chromone (Figure S14a), the time-dependent fluorescence intensities (Figure S14b) and absorbance properties (Figure S14c) observed at 460 nm and 436 nm respectively were recorded to evaluate the response time and stability toward different amounts of EDA solutions (100, 300, and 500 μM). Upon the addition of EDA, the fluorescence intensities increase gradually when the concentration of EDA is 100 μM (green dots line). As the concentration increases (orange and purple dots lines), the fluorescence intensities increase rapidly within 30 s and basically reach saturation after 100 s, and then decrease gently afterwards, which might be due to the formation of dimer in the generation of the expanded conjugated fluorophores grafted on QDs (QDs-H-CF). And the van der Waals interaction between the planes becomes more significant (Figure S15), especially in the presence of relatively high concentrations of EDA. The time-dependent absorbance properties are similar to that of the fluorescence change feature, and the absorbance also increases gradually when the concentration of EDA is 100 μM (green dots line). And similarly, as the concentration increases (orange and purple dots line), the absorbance increases rapidly within 20 s and then reaches to a nearly saturation state after 30 s, and also decreases slowly afterwards. Thus, based on the EET mechanism of the present QDs-Chromone in the detection of EDA, a fluorescent and colorimetric dual-mode detection strategy toward trace analyte was established with ultrasensitive, specific as well as rapid and stable performance.

Highly Selective Distinguishing Performance and Mechanism. To further investigate the specificity of the QDs-Chromone toward EDA, the structural analogues (various amines), inorganic salt (including alkaline and hazardous), common explosives, organic acid, and common daily necessities were selected as potential interferents. For structural analogues, considering the steric hindrance, nucleophilicity, and the quantity of H on the N of the amines, five different kinds of structural analogues were chosen (Figure 5a). EDA (1), 1,2-propylamine (2), 1,5-diaminopentane (3), and 1,12-diaminododecane (4) represent the aliphatic diamines with different chains of carbon atoms, while cyclohexylamine (5), aniline (6), *p*-toluidine (7), *tert*-butylamine (8), L-cysteine (9), and hydrazine hydrate (10) are chosen for the different steric hindrance. Meanwhile, it is noteworthy to investigate that whether the presence of the O atom in acrylamide (11) and urea (12) would affect the nucleophilicity of the amidogen. Moreover, it is also worthy note to verify whether the secondary amines and tertiary amines, such as diethylamine (13), dipropylamine (14), diphenylamine (15), and triethylamine (16), N,N-diisopropylethylamine (17), urotropin (18), would interfere the distinguishing performance toward EDA.

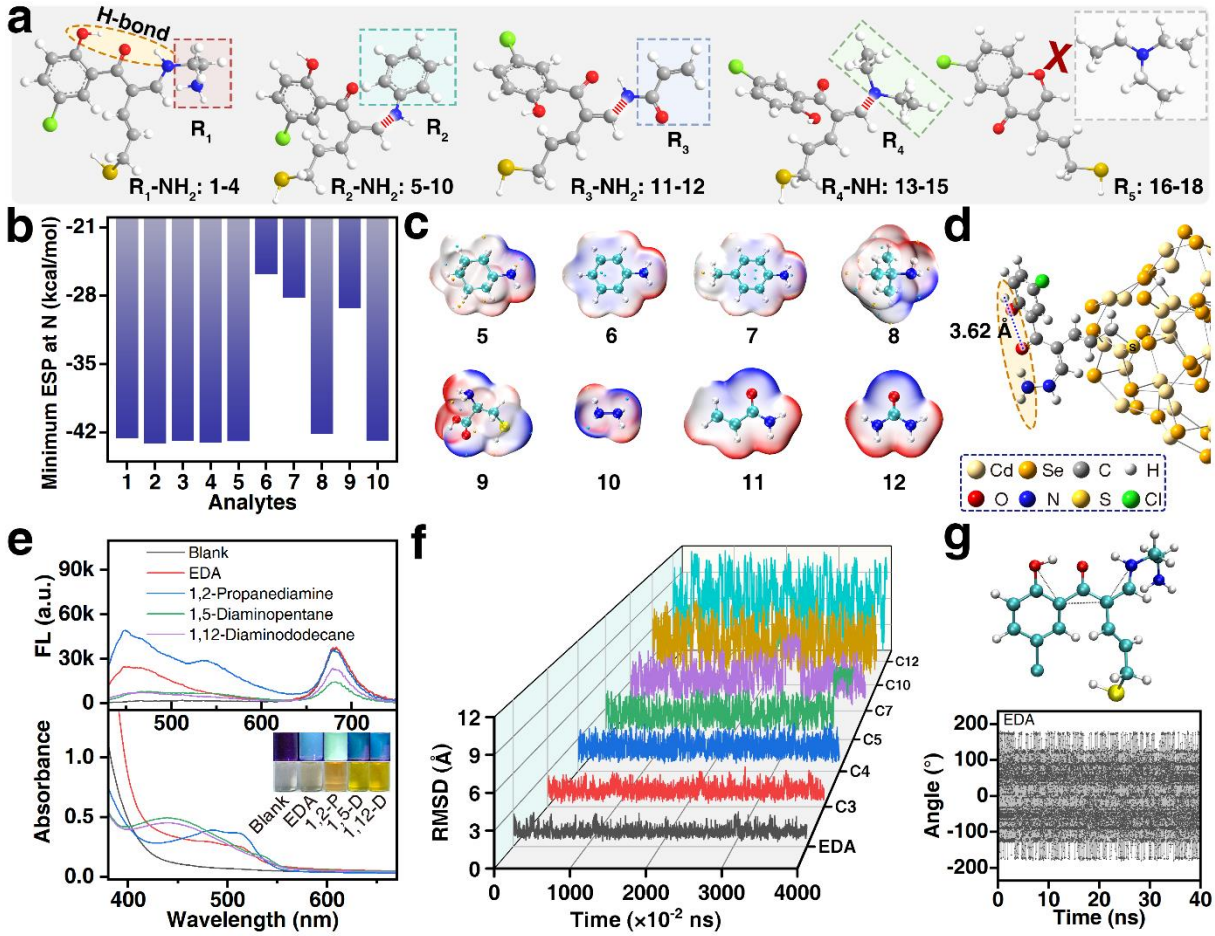

Figure 5. (a) The optimized structure of five different kinds of structural analogues after reaction with chromone. (1) EDA, (2) 1,2-propylamine, (3) 1,5-diaminopentane, (4) 1,12-diaminododecane, (5) cyclohexylamine, (6) aniline, (7) *p*-toluidine, (8) *tert*-butylamine, (9) L-cysteine, (10) hydrazine hydrate, (11) acrylamide, (12) urea, (13) diethylamine, (14) dipropylamine, (15) diphenylamine, (16) triethylamine, (17) N,N-diisopropylethylamine, (18) urotropin. (b) Minimum electrostatic potential (ESP) at N atoms of amines. (c) ESP diagram with the penetration of van der Waals surface. (d) The optimized structure of hydrazine hydrate after reacting with the QDs-Chromone. (e) Relative fluorescence intensity and absorbance of the QDs-Chromone solution towards four different diamines (1-4). (f) The root mean square displacement/deviation (RMSD) of chromone ligand after reaction with EDA, 1,3-propanediamine (C3), 1,4-diaminobutane (C4), 1,5-diaminopentane (C5), 1,7-diaminoheptane (C7), 1,10-diaminodecane (C10), and 1,12-diaminododecane (C12) as a function of simulation time, respectively. (g) The schematic illustration of the dihedral angle and the its variation with time for the chromone ligand after reaction with EDA.

By means of the ESP analysis, the nucleophilicity of the amines could be displayed visually (Figure 5b and S16). It is found that the minimum ESP[58] contributed by the lone pair electrons of the N atoms in the aliphatic diamines (Figure 5b 1-4) as well as cyclohexylamine (5), *tert*-butylamine (8), and hydrazine hydrate (10) has a value around -42 kcal/mol, respectively, representing that all of them have a more favorable nucleophilicity. However, due to the high steric hindrance of the hexatomic ring and branches, which can be seen from the molecular structures (Figure 5c), cyclohexylamine (5) and *tert*-butylamine (8) are hard to react with the QDs-Chromone, as well as aniline (6), *p*-toluidine (7), and L-cysteine (9). As for amides, due to the global minimum ESP generated at the lone pair electron of its O atom, the strongest electrostatic attraction of the O atom in the reaction process will preferentially bind with the QDs-Chromone rather than the amidogen, which greatly reduces the possibility of amides' nucleophilic reaction with the QDs-chromone (Figure 5c 11-12). However, as a compound with low steric hindrance and high nucleophilicity, hydrazine hydrate (10) cannot form the stable hydrogen bonds (O–H···O) after reacting with the QDs-Chromone due to the excessive distance (3.62 Å) between the O atom and the H atom,[59] since the two high nucleophilicity of N atoms in hydrazine hydrate are too close (Figure 5d).

The conclusion of aliphatic diamines has been verified by the corresponding fluorescence spectra and images (Figure 5e), in which dramatic fluorescence transformation can be observed for EDA and 1,2-propylamine. However, the fluorescence changes of them are different, which is from red to blue and from red to cyan for them, respectively. It is considered that the extra methyl of 1,2-propylamine may result in different product molecular configurations after detection. Noticeably, EDA exhibits the strongest fluorescence intensity at 460 nm compared to the other two aliphatic diamines (1,5-diaminopentane and 1,12-diaminododecane), which means the formation of the two kinds of hydrogen bonds is the most stable. At the same time, except for EDA, all the distinguishment toward

other diamines appeared a distinct yellow color change after reaction with the QDs-Chromone, and the appearance of this yellow color could be attributed to the absorption in the blue range and consequently the relatively weak blue fluorescence for them could be observed. Therefore, the colorimetric mode can assist in the screening of diamines. By analyzing the root mean square displacement/deviation (RMSD) of the product for the chromone ligand reacting with diamines (EDA, C3, C4, C5, C7, C10, C12) of different alkyl chain lengths, it is found that the fluctuation of the product induced by EDA is the lowest, indicating the corresponding energy dissipation of the thermal motion is the minimal (Figure 5f and S17). By comparing the corresponding fluctuations of the dihedral angles these reaction products, it is also found that the dihedral angle for the EDA-induced product is the most stable one, proving the favourable stable conjugation and thus the brightest fluorescence emission (Figure 5g and S18).

As expected, the amides, and the secondary amines as well as the tertiary amines cannot cause the fluorescence transformation, which could be ascribed to the shielding effect of the O atoms and the relatively weak alkalinity,[45] respectively. Additionally, the coloring change (from almost transparent and colorless to orange) can also be observed after the addition of certain amines, implying that the selectivity of the colorimetric mode is not superior comparing to the fluorescent mode (Figure S19). As for the anti-interference performances in the presence of these amines, the characteristic yellow color was not disturbed by all of the 17 amines, but with an enhanced yellow signal in the colorimetric mode. It is also desirable by directly observing the fluorescent mode with a characteristic blue emission except for aliphatic diamines (2-4) (Figure S20a-b). Although the anti-interference performances in the presence of aliphatic diamines in the fluorescent mode was different from others, the discrimination of EDA can be realized with the relatively specific fluorescence, which is a blue fluorescence resulted from EDA mixed with the fluorescence resulted from the other corresponding aliphatic diamine. Based on the logical judgment with the flow chart in Figure S20c, whether EDA exist when aliphatic diamines (2-4) present as the interferents still can be judged. Nevertheless, it is hard to realize the precise quantitative detection of EDA in the complex medium with these interferents. Besides, for the inorganic salts, common explosives, organic acids, and common daily necessities, although the color changes towards some alkaline inorganic salts and colored interferents, the fluorescence of the QDs-Chromone have no similar changes from red to blue (Figure S21). Apparently, from the aspects of response time, LOD, and selectivity, the QDs-Chromone based on the nucleophilic attack of EDA towards the chromone has better on-site distinguishing performance than those of the previously reported fluorescence or colorimetry involved methods (Table S3). Thus, it can be concluded that based on the present EET mechanism, the QDs-Chromone is highly selective and specific to realize the distinguishment of EDA.

Superior Sensing Performance toward EDA Vapor. It is of great significance to screen the spillage events or terrorist activities especially for hazardous gas such as EDA.[6] A sensing platform of atmosphere with dual-mode response was established by adopting the polyurethane sponge with porous microstructure and excellent absorptivity as the support to immobilize the QDs-Chromone probe (Figure S22). The rosybrown emissive QDs-Chromone-based sensing chip under UV light could be constructed by simply trickling the QDs-Chromone solution into the pristine sponge, which was low cost. It can be observed that the Cl element is uniformly dispersed in the QDs-Chromone-based sensing chip, verifying the QDs-Chromone have been successfully embedded into the sponge (Figure S23). It is obviously observed that a fluorescence emission transformation from rosybrown to light blue and a color change from grayness to yellow due to the resultful assimilation and specific identification of the QDs-Chromone-based sensing chip towards EDA vapor (Figure 6a). Under an exposure duration of 60 s in different concentrations of EDA (3.5–560 ppm), both the fluorescent and colorimetric channels transformed gradually with the increase of the EDA concentration. This transformation trends can be extracted based on RGB value extraction and adequately described by the numerical analysis.[60-61] The gradual enhancement from 3.5 ppm to 105 ppm with a linear relationship is followed by a plateau from 105 ppm to 560 ppm both in the fluorescent and colorimetric channels, and the fluorescent mode shows even smaller data deviations (Figure 6b-c). This variation indicates that both the fluorescent and colorimetric channels possess a good quantification capability in a wide concentration range. Besides, it is clear that one can easily discriminate the existence of EDA vapor with a concentration as low as 10 ppm by naked-eye, which satisfies the exposure limit requirement for EDA vapor monitoring stated by the WHO (25 mg/m^3, ~10 ppm).[7]

Additionally, structural analogues, common explosives, organic acids, organic solvents in laboratory and liquid daily products were selected as the potential interferents to investigate the specificity and the anti-interference performance of the QDs-Chromone-based sensing chip towards the EDA vapor and the gas of the ordinary volatile substances (Figure S24). It is shown that although the perf-

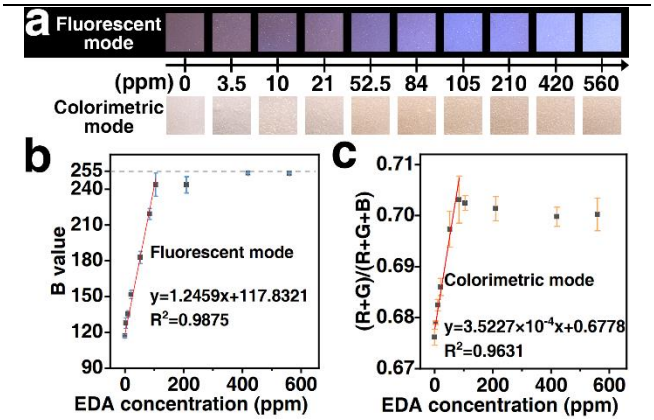

Figure 6. (a) The fluorescent and colorimetric images of the QDs-Chromone-based sensing chip for detecting different concentrations of EDA vapor. The plotting curves of (b) B value and (c) (R+G)/(R+G+B) value extracted from the QDs-Chromone-based sensing chip versus the different EDA concentrations.

ormance of the colorimetric channel is relatively poor, only the occurrence of the EDA vapor can lead to the transformation in the fluorescence emission from rosybrown to light blue, demonstrating the superiority of the dual-mode design. No matter for individual interferents or for the coexisting interferents, the EET mechanism ensures the superior dual-mode sensing for EDA monitoring and thus is promising to be employed in complicated application scenarios.

CONCLUSION

In conclusion, we pioneeringly constructed the highly efficient EET without the spectral overlap in functionalized QDs drived by analytes, which was further utilized to detect trace EDA ultrasensitively and specifically. This strategy is demonstrated to effective in semiquantitatively detecting EDA, including both solution and vapor, with fluorescent and colorimetric dual-mode responses. The two emission peaks resulted in the internal referencing of the signal and a distinguishable emission transition from red to blue with a LOD (0.11 μM), the selectivity of which can be further promoted by the colorimetric mode. In addition, we showed an accessible identification by naked-eye toward 10 ppm EDA vapor and excellent specificity facing with potential co-existing gaseous substances. We expect this tentative study on EET would pave a new way for establishing effective interaction with the target analyte and greatly advance the exploration of functionalized QDs for various applications.

CALCULATION METHOD

The theoretical calculation in this work was performed by the Gaussian 09 C01.[62] Subsequently, the Multiwfn was used to analyze the wave function.[63] The VMD program was used to render the corresponding graphic picture.[64] All geometric structure optimization tasks of computational models related to QDs were completed by CP2K 2023.1 package.[65] The conformational distribution of the constructure was determined based on Gibbs free energy calculations using Gentor/Molclus[66]/Gaussian/ORCA[67-68] software. All molecular dynamics (MD) simulations were performed using the GROMACS 2023.2.[69-70] More details are provided in the Supporting Information.

ASSOCIATED CONTENT

The Supporting Information is available free of charge at http://pubs.acs.org.

Materials and methods, synthetic scheme, computation details, preparation of samples and testing process, and the corresponding charts associated with the manuscript (PDF)

AUTHOR INFORMATION

Corresponding Authors

Baiyi Zu – *Xinjiang Key Laboratory of Trace Chemicals Sensing, Xinjiang Technical Institute of Physics and Chemistry, Chinese Academy of Sciences, Urumqi 830011, China; Key Laboratory of Improvised Explosive Chemicals for State Market Regulation, Urumqi 830011, China;* Email: byzu@ms.xjb.ac.cn

Xincun Dou – *Xinjiang Key Laboratory of Trace Chemicals Sensing, Xinjiang Technical Institute of Physics and Chemistry, Chinese Academy of Sciences, Urumqi 830011, China; Center of Materials Science and Optoelectronics Engineering, University of Chinese Academy of Sciences, Beijing 100049, China; Key Laboratory of Improvised Explosive Chemicals for State Market Regulation, Urumqi 830011, China;* orcid.org/0000-0001-5825-9937; Email: xcdou@ms.xjb.ac.cn

Authors

Wenfei Ren – *Xinjiang Key laboratory of Trace Chemicals Sensing, Xinjiang Technical Institute of Physics and Chemistry, Chinese Academy of Sciences, Urumqi 830011, China; Center of Materials Science and Optoelectronics Engineering, University of Chinese Academy of Sciences, Beijing 100049, China*

Jiguang Li – *Xinjiang Key laboratory of Trace Chemicals Sensing, Xinjiang Technical Institute of Physics and Chemistry, Chinese Academy of Sciences, Urumqi 830011, China*

Da Lei – *Xinjiang Key laboratory of Trace Chemicals Sensing, Xinjiang Technical Institute of Physics and Chemistry, Chinese Academy of Sciences, Urumqi 830011, China; Key Laboratory of Improvised Explosive Chemicals for State Market Regulation, Urumqi 830011, China*

Author Contributions

‡These authors contributed equally.

Notes

The authors declare no competing financial interest.

ACKNOWLEDGMENT

This work is financially supported by the funders of National Natural Science Foundation of China (U1903306, 52172168, 61971416), Natural Science Foundation of Xinjiang (2021D01D04), Tianshan Innovation Team Plan (2022TSYCTD0020), Key Research Program of Frontier Sciences (CAS Grant No. ZDBS-LY-JSC029), and the Youth Innovation Promotion Association, CAS (Y2022106).

REFERENCES

1. Kumar, R.; Flodén, N. J.; Whitehurst, W. G.; Gaunt, M. J. A general carbonyl alkylative amination for tertiary amine synthesis. *Nature* **2020,** *581* (7809), 415-420. DOI: 10.1038/s41586-020-2213-0.
2. Froidevaux, V.; Negrell, C.; Caillol, S.; Pascault, J.-P.; Boutevin, B. Biobased amines: From synthesis to polymers; present and future. *Chem. Rev.* **2016,** *116* (22), 14181-14224. DOI: 10.1021/acs.chemrev.6b00486.
3. Xi, Y.; Ma, S.; Hartwig, J. F. Catalytic asymmetric addition of an amine N–H bond across internal alkenes. *Nature* **2020,** *588* (7837), 254-260. DOI: 10.1038/s41586-020-2919-z.
4. Jia, R.; Tian, W.; Bai, H.; Zhang, J.; Wang, S.; Zhang, J. Amine-responsive cellulose-based ratiometric fluorescent materials for real-time and visual detection of shrimp and crab freshness. *Nat. Commun.* **2019,** *10* (1), 795. DOI: 10.1038/s41467-019-08675-3.
5. Wang, J.; Li, D.; Ye, Y.; Qiu, Y.; Liu, J.; Huang, L.; Liang, B.; Chen, B. A fluorescent metal–organic framework for food real-time visual monitoring. *Adv. Mater.* **2021,** *33* (15), 2008020. DOI: 10.1002/adma.202008020.
6. Ke, Y.; Liu, Y.; Zu, B.; Lei, D.; Wang, G.; Li, J.; Ren, W.; Dou, X. Electronic tuning in reaction-based fluorescent sensing for instantaneous and ultrasensitive visualization of ethylenediamine. *Angew. Chem. Int. Ed.* **2022,** *134*, e202203358. DOI: 10.1002/anie.202203358.
7. Cary, R.; Dobson, S.; Delic, J.; World Health, O.; International Programme on Chemical, S., 1,2-diaminoethane (ethylenediamine). World Health Organization: Geneva, 1999.

8. Ma, Z.; Li, J.; Hu, X.; Cai, Z.; Dou, X. Ultrasensitive, specific, and rapid fluorescence turn-on nitrite sensor enabled by precisely modulated fluorophore binding. *Adv. Sci.* **2020,** *7* (24), 2002991. DOI: 10.1002/advs.202002991.
9. Su, Z.; Li, Y.; Li, J.; Li, K.; Dou, X. Ultrasensitive dual-mode visualization of perchlorate in water, soil and air boosted by close and stable Pt-Pt packing endowed low-energy absorption and emission. *J. Mater. Chem. A* **2022,** *10*, 8195-8207. DOI: 10.1039/D2TA00843B.
10. Wang, G.; Wan, Z.; Cai, Z.; Li, J.; Li, Y.; Hu, X.; Lei, D.; Dou, X. Complete inhibition of the rotation in a barrierless TICT probe for fluorescence-on qualitative analysis. *Anal. Chem.* **2022,** *94* (33), 11679-11687. DOI: 10.1021/acs.analchem.2c02407.
11. Li, J.; Lei, D.; Ma, Z.; Zu, B.; Dou, X. A general twisted intramolecular charge transfer triggering strategy by protonation for zero-background fluorescent turn-on sensing. *J. Phys. Chem. Lett.* **2022,** *13* (46), 10871-10881. DOI: 10.1021/acs.jpclett.2c02847.
12. Wang, G.; Liu, Y.; Zu, B.; Lei, D.; Guo, Y.; Wang, M.; Dou, X. Reversible adhesive hydrogel with enhanced sampling efficiency boosted by hydrogen bond and van der Waals force for visualized detection. *Chem. Eng. J.* **2023,** *455*, 140493. DOI: 10.1016/j.cej.2022.140493.
13. Qin, J.; Li, X.; Cao, L.; Du, S.; Wang, W.; Yao, S. Q. Competition-based universal photonic crystal biosensors by using antibody–antigen interaction. *J. Am. Chem. Soc.* **2020,** *142* (1), 417-423. DOI: 10.1021/jacs.9b11116.
14. Liu, K.; Shang, C.; Wang, Z.; Qi, Y.; Miao, R.; Liu, K.; Liu, T.; Fang, Y. Non-contact identification and differentiation of illicit drugs using fluorescent films. *Nat. Commun.* **2018,** *9* (1), 1695. DOI: 10.1038/s41467-018-04119-6.
15. Li, W.; Wang, J.; Li, C.; Zong, Z.; Zhao, J.; Gao, H.; Liu, D. Achieving ultrasensitive chromogenic probes for rapid, direct detection of carbapenemase-producing bacteria in sputum. *JACS Au* **2023,** *3* (1), 227-238. DOI: 10.1021/jacsau.2c00607.
16. Miao, X.; Wu, C.; Li, F.; Zhang, M. Fast and visual detection of biogenic amines and food freshness based on ICT-induced ratiometric fluorescent probes. *Adv. Funct. Mater.* **2023,** *33*, 2212980. DOI: 10.1002/adfm.202212980.
17. Zheng, Z.; Yu, H.; Geng, W.; Hu, X.; Wang, Y.; Li, Z.; Wang, Y.; Guo, D. Guanidinocalix[5]arene for sensitive fluorescence detection and magnetic removal of perfluorinated pollutants. *Nat. Commun.* **2019,** *10* (1), 5762. DOI: 10.1038/s41467-019-13775-1.
18. Wang, G.; Li, Y.; Cai, Z.; Dou, X. A colorimetric artificial olfactory system for airborne improvised explosive identification. *Adv. Mater.* **2020,** *32* (14), 1907043. DOI: 10.1002/adma.201907043.
19. Dai, Z.; Wang, G.; Xiao, F.; Lei, D.; Dou, X. Amorphous copper-based nanoparticles with clusterization-triggered phosphorescence for ultrasensing 2,4,6-trinitrotoluene. *Adv. Mater.* **2023,** *35*, 2300526. DOI: 10.1002/adma.202300526.
20. Zhang, K.; Zhou, H.; Mei, Q.; Wang, S.; Guan, G.; Liu, R.; Zhang, J.; Zhang, Z. Instant visual detection of trinitrotoluene particulates on various surfaces by ratiometric fluorescence of dual-emission quantum dots hybrid. *J. Am. Chem. Soc.* **2011,** *133* (22), 8424-8427. DOI: 10.1021/ja2015873.
21. Lim, S. H.; Feng, L.; Kemling, J. W.; Musto, C. J.; Suslick, K. S. An optoelectronic nose for the detection of toxic gases. *Nat. Chem.* **2009,** *1* (7), 562-567. DOI: 10.1038/nchem.360.
22. Jia, Y.; Hu, J.-P.; Dang, L.-R.; Yao, H.; Shi, B.; Zhang, Y.-M.; Wei, T.-B.; Lin, Q. Rational tuning of binding properties of pillar[5]arene-based crystalline material by synergistic effect and its application for fluorescent detection and adsorption of 1,2-ethylenediamine. *ACS Sustainable Chem. Eng.* **2021,** *9* (48), 16203-16209. DOI: 10.1021/acssuschemeng.1c05451.
23. Li, E.; Jie, K.; Fang, Y.; Cai, P.; Huang, F. Transformation of nonporous adaptive pillar[4]arene[1]quinone crystals into fluorescent crystals via multi-step solid–vapor postsynthetic modification for fluorescence turn-on sensing of ethylenediamine. *J. Am. Chem. Soc.* **2020,** *142* (36), 15560-15568. DOI: 10.1021/jacs.0c07482.
24. Chuang, P.; Tu, Y.; Wu, J. A thiadiazole-functionalized Zn(II)-based luminescent coordination polymer with seven-fold interweaved herringbone nets showing solvent-responsive fluorescence properties and discriminative detection of ethylenediamine. *Sens. Actuators, B* **2022,** *366*, 131967. DOI: 10.1016/j.snb.2022.131967.
25. Zhang, X.; Zhu, W.; Yang, Z.; Feng, Y.; Fan, L.; Gao, G.; Liu, H. Ultrasensitive photochromic and Raman dual response to ethylenediamine gas through polyoxometalate–viologen crystalline hybrid. *J. Mater. Chem. C* **2022,** *10* (41), 15451-15457. DOI: 10.1039/D2TC03053E.
26. Li, W.; Kaminski Schierle, G. S.; Lei, B.; Liu, Y.; Kaminski, C. F. Fluorescent nanoparticles for super-resolution imaging. *Chem. Rev.* **2022,** *122* (15), 12495-12543. DOI: 10.1021/acs.chemrev.2c00050.
27. Hildebrandt, N.; Spillmann, C. M.; Algar, W. R.; Pons, T.; Stewart, M. H.; Oh, E.; Susumu, K.; Diaz, S. A.; Delehanty, J. B.; Medintz, I. L. Energy transfer with semiconductor quantum dot bioconjugates: A versatile platform for biosensing, energy harvesting, and other developing applications. *Chem. Rev.* **2017,** *117* (2), 536-711. DOI: 10.1021/acs.chemrev.6b00030.
28. Baek, W.; Chang, H.; Bootharaju, M. S.; Kim, J. H.; Park, S.; Hyeon, T. Recent advances and prospects in colloidal nanomaterials. *JACS Au* **2021,** *1* (11), 1849-1859. DOI: 10.1021/jacsau.1c00339.
29. Heuer-Jungemann, A.; Feliu, N.; Bakaimi, I.; Hamaly, M.; Alkilany, A.; Chakraborty, I.; Masood, A.; Casula, M. F.; Kostopoulou, A.; Oh, E.; Susumu, K.; Stewart, M. H.; Medintz, I. L.; Stratakis, E.; Parak, W. J.; Kanaras, A. G. The role of ligands in the chemical synthesis and applications of inorganic nanoparticles. *Chem. Rev.* **2019,** *119* (8), 4819-4880. DOI: 10.1021/acs.chemrev.8b00733.
30. Silvi, S.; Credi, A. Luminescent sensors based on quantum dot–molecule conjugates. *Chem. Soc. Rev.* **2015,** *44* (13), 4275-4289. DOI: 10.1039/C4CS00400K.
31. Resch-Genger, U.; Grabolle, M.; Cavaliere-Jaricot, S.; Nitschke, R.; Nann, T. Quantum dots versus organic dyes as fluorescent labels. *Nat. Methods* **2008,** *5* (9), 763-775. DOI: 10.1038/nmeth.1248.
32. Algar, W. R.; Hildebrandt, N.; Vogel, S. S.; Medintz, I. L. FRET as a biomolecular research tool — understanding its potential while avoiding pitfalls. *Nat. Methods* **2019,** *16* (9), 815-829. DOI: 10.1038/s41592-019-0530-8.
33. Ye, Y.; Wu, T.; Jiang, X.; Cao, J.; Ling, X.; Mei, Q.; Chen, H.; Han, D.; Xu, J.; Shen, Y. Portable smartphone-based QDs for the visual onsite monitoring of fluoroquinolone antibiotics in actual food and environmental samples. *ACS Appl. Mater. Interfaces* **2020,** *12* (12), 14552-14562. DOI: 10.1021/acsami.9b23167.
34. Sheng, E.; Lu, Y.; Tan, Y.; Xiao, Y.; Li, Z.; Dai, Z. Ratiometric fluorescent quantum dot-based biosensor for chlorothalonil detection via an inner-filter effect. *Anal. Chem.* **2020,** *92* (6), 4364-4370. DOI: 10.1021/acs.analchem.9b05199.
35. Algar, W. R.; Khachatrian, A.; Melinger, J. S.; Huston, A. L.; Stewart, M. H.; Susumu, K.; Blanco-Canosa, J. B.; Oh, E.; Dawson, P. E.; Medintz, I. L. Concurrent modulation of quantum dot photoluminescence using a combination of charge transfer and Förster resonance energy transfer: Competitive quenching and multiplexed biosensing modality. *J. Am. Chem. Soc.* **2017,** *139* (1), 363-372. DOI: 10.1021/jacs.6b11042.
36. Guo, X.; Huang, J.; Zeng, Q.; Wei, Y.; Liu, X.; Wang, L. Boronic acid-functionalized molybdenum disulfide quantum dots for the ultrasensitive analysis of dopamine based on synergistic quenching effects from IFE and aggregation. *J. Mater. Chem. B* **2019,** *7* (17), 2799-2807. DOI: 10.1039/C9TB00019D.
37. Tang, G.; Du, L.; Su, X. Detection of melamine based on the fluorescence resonance energy transfer between CdTe QDs and

Rhodamine B. *Food Chem.* **2013,** *141* (4), 4060-4065. DOI: 10.1016/j.foodchem.2013.06.135.
38. Shi, L.; Yan, C.; Guo, Z.; Chi, W.; Wei, J.; Liu, W.; Liu, X.; Tian, H.; Zhu, W. De novo strategy with engineering anti-Kasha/Kasha fluorophores enables reliable ratiometric quantification of biomolecules. *Nat. Commun.* **2020,** *11* (1), 793. DOI: 10.1038/s41467-020-14615-3.
39. Becker, K.; Lupton, J. M.; Feldmann, J.; Setayesh, S.; Grimsdale, A. C.; Müllen, K. Efficient intramolecular energy transfer in single endcapped conjugated polymer molecules in the absence of appreciable spectral overlap. *J. Am. Chem. Soc.* **2006,** *128* (3), 680-681. DOI: 10.1021/ja056469h.
40. Athanasopoulos, S.; Alfonso Hernandez, L.; Beljonne, D.; Fernandez-Alberti, S.; Tretiak, S. Ultrafast non-Förster intramolecular donor–acceptor excitation energy transfer. *J. Phys. Chem. Lett.* **2017,** *8* (7), 1688-1694. DOI: 10.1021/acs.jpclett.7b00259.
41. Wiebeler, C.; Plasser, F.; Hedley, G. J.; Ruseckas, A.; Samuel, I. D. W.; Schumacher, S. Ultrafast electronic energy transfer in an orthogonal molecular dyad. *J. Phys. Chem. Lett.* **2017,** *8* (5), 1086-1092. DOI: 10.1021/acs.jpclett.7b00089.
42. Patalag, L. J.; Hoche, J.; Holzapfel, M.; Schmiedel, A.; Mitric, R.; Lambert, C.; Werz, D. B. Ultrafast resonance energy transfer in ethylene-bridged BODIPY heterooligomers: From Frenkel to Förster coupling limit. *J. Am. Chem. Soc.* **2021,** *143* (19), 7414-7425. DOI: 10.1021/jacs.1c01279.
43. He, X.; Zhang, J.; Liu, X.; Jin, Z.; Lam, J. W. Y.; Tang, B. Z. A multiresponsive functional AIEgen for spatiotemporal pattern control and all-round information encryption. *Angew. Chem. Int. Ed.* **2023,** *62* (18), e202300353. DOI: 10.1002/anie.202300353.
44. He, X.; Xie, H.; Hu, L.; Liu, P.; Xu, C.; He, W.; Du, W.; Zhang, S.; Xing, H.; Liu, X.; Park, H.; Cheung, T. S.; Li, M.-H.; Kwok, R. T. K.; Lam, J. W. Y.; Lu, J.; Tang, B. Z. A versatile AIE fluorogen with selective reactivity to primary amines for monitoring amination, protein labeling, and mitochondrial staining. *Aggregate* **2023,** *4* (1), e239. DOI: 10.1002/agt2.239.
45. Kemp, D. S.; Hanson, G. New protective groups for peptide synthesis. 4. Chromone-derived protection for amine and carboxyl functions. *J. Org. Chem.* **1981,** *46* (24), 4971-4975. DOI: 10.1021/jo00337a030.
46. Sosnovskikh, V. Y.; Moshkin, V. S.; Kodess, M. I. Structural revision in the reactions of 3-cyanochromones with primary aromatic amines. Improved synthesis of 2-amino-3-(aryliminomethyl)chromones. *Tetrahedron Lett.* **2009,** *50* (47), 6515-6518. DOI: 10.1016/j.tetlet.2009.09.028.
47. Smith, A. M.; Nie, S. Semiconductor nanocrystals: Structure, properties, and band gap engineering. *Acc. Chem. Res.* **2010,** *43* (2), 190-200. DOI: 10.1021/ar9001069.
48. Feng, G.; Zhang, G.; Ding, D. Design of superior phototheranostic agents guided by Jablonski diagrams. *Chem. Soc. Rev.* **2020,** *49* (22), 8179-8234. DOI: 10.1039/D0CS00671H.
49. Altintas, Y.; Genc, S.; Talpur, M. Y.; Mutlugun, E. CdSe/ZnS quantum dot films for high performance flexible lighting and display applications. *Nanotechnology* **2016,** *27* (29), 295604. DOI: 10.1088/0957-4484/27/29/295604.
50. Zhou, J.; Pu, C.; Jiao, T.; Hou, X.; Peng, X. A two-step synthetic strategy toward monodisperse colloidal CdSe and CdSe/CdS core/shell nanocrystals. *J. Am. Chem. Soc.* **2016,** *138* (20), 6475-6483. DOI: 10.1021/jacs.6b00674.
51. Han, Y.; Chen, Y.; Feng, J.; Liu, J.; Ma, S.; Chen, X. One-pot synthesis of fluorescent silicon nanoparticles for sensitive and selective determination of 2,4,6-trinitrophenol in aqueous solution. *Anal. Chem.* **2017,** *89* (5), 3001-3008. DOI: 10.1021/acs.analchem.6b04509.
52. Li, C.; Xu, X.; Wang, F.; Zhao, Y.; Shi, Y.; Zhao, X.; Liu, J. Portable smartphone platform integrated with paper strip-assisted fluorescence sensor for ultrasensitive and visual quantitation of ascorbic acid. *Food Chem.* **2023,** *402*, 134222. DOI: 10.1016/j.foodchem.2022.134222.
53. Prusti, B.; Tripathi, S.; Jain, A.; Chakravarty, M. Concentration-guided visual detection of multiphase aliphatic biogenic amines through amine–phenol recognition using a dual-state emitter. *ACS Appl. Mater. Interfaces* **2023,** *15* (13), 16492-16504. DOI: 10.1021/acsami.3c00791.
54. Kilina, S. V.; Tamukong, P. K.; Kilin, D. S. Surface chemistry of semiconducting quantum dots: Theoretical perspectives. *Acc. Chem. Res.* **2016,** *49* (10), 2127-2135. DOI: 10.1021/acs.accounts.6b00196.
55. Kasha, M. Characterization of electronic transitions in complex molecules. *Discuss. Faraday. Soc.* **1950,** *9* (9), 14-19. DOI: 10.1039/df9500900014.
56. Liu, Z.; Lu, T.; Chen, Q. An sp-hybridized all-carboatomic ring, cyclo[18]carbon: Electronic structure, electronic spectrum, and optical nonlinearity. *Carbon* **2020,** *165*, 461-467. DOI: 10.1016/j.carbon.2020.05.023.
57. Yuan, J.; Yuan, Y.; Tian, X.; Liu, Y.; Sun, J. Insights into the photobehavior of fluorescent oxazinone, quinazoline, and difluoroboron derivatives: Molecular design based on the structure–property relationships. *J. Phys. Chem. C.* **2017,** *121* (14), 8091-8108. DOI: 10.1021/acs.jpcc.7b01360.
58. Lu, T.; Chen, F. Quantitative analysis of molecular surface based on improved marching tetrahedra algorithm. *J. Mol. Graphics Modell.* **2012,** *38*, 314-323. DOI: 10.1016/j.jmgm.2012.07.004.
59. Perrin, C. L.; Nielson, J. B. "Strong" hydrogen bonds in chemistry and biology. *Annu. Rev. Phys. Chem.* **1997,** *48* (1), 511-544. DOI: 10.1146/annurev.physchem.48.1.511.
60. Wang, G.; Cai, Z.; Dou, X. Colorimetric logic design for rapid and precise discrimination of nitrate-based improvised explosives. *Cell Rep. Phys. Sci.* **2021,** *2* (2), 100317. DOI: 10.1016/j.xcrp.2020.100317.
61. Woolf, M. S.; Dignan, L. M.; Scott, A. T.; Landers, J. P. Digital postprocessing and image segmentation for objective analysis of colorimetric reactions. *Nat. Protoc.* **2021,** *16* (1), 218-238. DOI: 10.1038/s41596-020-00413-0.
62. Frisch, M. J.; Trucks, G. W.; Schlegel, H. B.; Scuseria, G. E.; Robb, M. A.; Cheeseman, J. R.; Scalmani, G.; Barone, V.; Petersson, G. A.; Nakatsuji, H.; Li, X.; Caricato, M.; Marenich, A. V.; Bloino, J.; Janesko, B. G.; Gomperts, R.; Mennucci, B.; Hratchian, H. P.; Ortiz, J. V.; Izmaylov, A. F.; Sonnenberg, J. L.; Williams; Ding, F.; Lipparini, F.; Egidi, F.; Goings, J.; Peng, B.; Petrone, A.; Henderson, T.; Ranasinghe, D.; Zakrzewski, V. G.; Gao, J.; Rega, N.; Zheng, G.; Liang, W.; Hada, M.; Ehara, M.; Toyota, K.; Fukuda, R.; Hasegawa, J.; Ishida, M.; Nakajima, T.; Honda, Y.; Kitao, O.; Nakai, H.; Vreven, T.; Throssell, K.; Montgomery Jr., J. A.; Peralta, J. E.; Ogliaro, F.; Bearpark, M. J.; Heyd, J. J.; Brothers, E. N.; Kudin, K. N.; Staroverov, V. N.; Keith, T. A.; Kobayashi, R.; Normand, J.; Raghavachari, K.; Rendell, A. P.; Burant, J. C.; Iyengar, S. S.; Tomasi, J.; Cossi, M.; Millam, J. M.; Klene, M.; Adamo, C.; Cammi, R.; Ochterski, J. W.; Martin, R. L.; Morokuma, K.; Farkas, O.; Foresman, J. B.; Fox, D. J. *Gaussian 09 Rev. C.01*, Wallingford, CT, 2009.
63. Lu, T.; Chen, F. Multiwfn: A multifunctional wavefunction analyzer. *J. Comput. Chem.* **2012,** *33* (5), 580-592. DOI: 10.1002/jcc.22885.
64. Humphrey, W.; Dalke, A.; Schulten, K. VMD: Visual molecular dynamics. *J. Mol. Graphics Modell.* **1996,** *14* (1), 33-38. DOI: 10.1016/0263-7855(96)00018-5.
65. Kühne, T. D.; Iannuzzi, M.; Ben, M. D.; Rybkin, V. V.; Seewald, P.; Stein, F.; Laino, T.; Khaliullin, R. Z.; Schütt, O.; Schiffmann, F.; Golze, D.; Wilhelm, J.; Chulkov, S.; Bani-Hashemian, M. H.; Weber, V.; Borštnik, U.; Taillefumier, M.; Jakobovits, A. S.; Lazzaro, A.; Pabst, H.; Müller, T.; Schade, R.; Guidon, M.; Andermatt, S.; Holmberg, N.; Schenter, G. K.; Hehn, A.; Bussy, A.; Belleflamme, F.; Tabacchi, G.; Glöß, A.; Lass, M.; Bethune, I.; Mundy, C. J.; Plessl, C.; Watkins, M.; VandeVondele, J.; Krack, M.; Hutter, J. CP2K: An electronic structure and molecular dynamics software package - quickstep: Efficient and accurate electronic structure calculations. *J. Chem. Phys.* **2020,** *152* (19), 194103. DOI: 10.1063/5.0007045.

66. Tian, L. *Molclus program, version 1.9.9.9*.
67. Neese, F. Software update: The ORCA program system, version 4.0. *WIREs Comput. Mol. Sci.* **2018,** *8* (1), e1327. DOI: 10.1002/wcms.1327.
68. Neese, F. Software update: The ORCA program system-version 5.0. *WIREs Comput. Mol. Sci.* **2022,** *12* (5), e1606. DOI: 10.1002/wcms.1606.
69. Abraham, M. J.; Murtola, T.; Schulz, R.; Páll, S.; Smith, J. C.; Hess, B.; Lindahl, E. GROMACS: High performance molecular simulations through multi-level parallelism from laptops to supercomputers. *SoftwareX* **2015,** *1-2*, 19-25. DOI: 10.1016/j.softx.2015.06.001.
70. Abraham, M.; Alekseenko, A.; Bergh, C.; Blau, C.; Briand, E.; Doijade, M.; Fleischmann, S.; Gapsys, V.; Garg, G.; Gorelov, S.; Gouaillardet, G.; Gray, A.; Irrgang, M. E.; Jalalypour, F.; Jordan, J.; Junghans, C.; Kanduri, P.; Keller, S.; Kutzner, C.; Lemkul, J. A.; Lundborg, M.; Merz, P.; Miletić, V.; Morozov, D.; Páll, S.; Schulz, R.; Shirts, M.; Shvetsov, A.; Soproni, B.; Spoel, D. v. d.; Turner, P.; Uphoff, C.; Villa, A.; Wingbermühle, S.; Zhmurov, A.; Bauer, P.; Hess, B.; Lindahl, E. GROMACS 2023.2 source code. **2023**. DOI: 10.5281/zenodo.8134397.

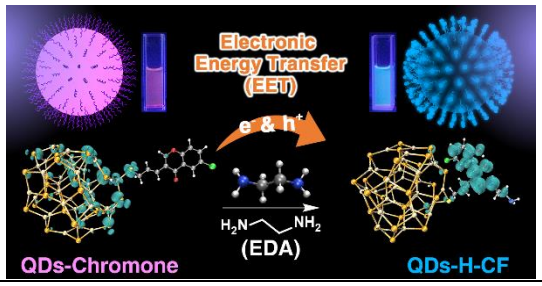
Electronic
Energy Transfer
(EET)
e⁻ & h⁺
H2N
NH2
(EDA)
QDs-Chromone
QDs-H-CF